Holocene forcing of East Asian hydroclimate recorded in a subtropical peatland from southeastern China

Xianyu Huang[1,2] · Hongbin Zhang[1] · Michael L. Griffiths[3] · Bingyan Zhao[1,7] · Francesco S. R. Pausata[4] · Clay Tabor[5] · Junwu Shu[6] · Shucheng Xie[1]

Abstract

The Holocene hydroclimate evolution and underlying mechanisms modulating the East Asian summer monsoon (EASM) remains controversial, especially in south eastern China. Here we present a multiproxy peat record of monsoon evolution from southeastern China covering the last 14 ka. Our new records show a relatively weaker EASM but wetter hydroclimate during the early (10 to 8 ka) and late Holocene (after 5.4 ka), while a stronger EASM and overall drier climate during the mid-Holocene (8 to 5.4 ka). In line with nearby speleothem records, our results reveal a dominant control of the northern-latitude ice-sheet meltwater forcing on millennial-scale East Asian hydroclimate variability during the last deglaciation and early Holocene. This dominant influence, however, likely waned once the global sea level had stabilized during the mid-to-late Holocene, giving way to other drivers of the monsoon and hydroclimate, including a combination of summer insolation and teleconnection patterns associated with vegetation-dust feedbacks.

1 Introduction

Hydrological changes associated with the East Asian summer monsoon (EASM) are essential for the terrestrial eco-systems and human societies in East Asia (Wang et al. 2017). A considerable number of studies, based on loess, lacustrine sediments, peat and cave deposits, have contributed to the significant advancement in our understanding of Holocene hydroclimate evolution across the greater EASM domain (Wang et al. 2005; Lu et al. 2013; Xie et al. 2013; Goldsmith et al. 2017; Zhu et al. 2017). However, these results show conflicting spatial patterns of hydroclimate, particularly along the monsoonal regions of eastern China (Rao et al. 2016). For example, widely distributed speleo-them records support an early-middle Holocene EASM maximum, which gradually became weaker following the decline in Northern Hemisphere summer insolation (Wang et al. 2005; Cheng et al. 2019). Meanwhile, numerous studies from northern China and southeastern China show that maximum EASM rainfall occurred during the mid-Holocene (Chen et al. 2015; Li et al. 2018a b; Wang and Huang 2019), while other records from the Yangtze River Valley (YRV) in

✉ Xianyu Huang
xyhuang@cug.edu.cn

✉ Hongbin Zhang
zhanghb@cug.edu.cn

1 State Key Laboratory of Biogeology and Environmental Geology, China University of Geosciences, Wuhan 430078, China

2 Hubei Key Laboratory of Critical Zone Evolution, School of Geography and Information Engineering, China University of Geosciences, Wuhan 430078, China

3 Department of Environmental Science, William Paterson University, Wayne, NJ 07470, USA

4 Centre ESCER (Etude Et La Simulation du Climat a; I'Echelle Regionale) and GEOTOP (Research Center on the Dynamics of the Earth System), Department of Earth and Atmospheric Sciences, University of Quebec in Montreal, Montreal, QC, Canada

5 Department of Geosciences, University of Connecticut, Storrs, CT, USA

6 Nanjing Institute of Geology and Palaeontology, Chinese Academy of Sciences, Nanjing 210008, China

7 Present Address: State Key Laboratory of Organic Geochemistry, Guangzhou Institute of Geochemistry, Chinese Academy of Sciences, Guangzhou 510640, People's Republic of China

central China show an opposing mid-Holocene drying trend (Xie et al. 2013; Zhu et al. 2017).

For areas to the south of the YRV, the paleoclimate history is more unclear because the relatively high rainfall and seasonal fluvial processes limit the continuous deposition of sedimentary sequences needed for paleoclimate reconstruction (Liu et al. 2014). Robust hydrological proxies are therefore scarce and temporally limited, restricting much of our current understanding of rainfall variability in central China to widely separated stalagmite $\delta^{18}O$ records (Wang et al. 2005; Hu et al. 2008; Yang et al. 2019). While these speleothem $\delta^{18}O$ records have shown to be a robust recorder of the Asian summer strength, they may not necessarily inform us of the local and regional hydroclimate (Liu et al. 2014; Zhang et al. 2018). To address these uncertainties, we present a novel multi-proxy paleohydrological reconstruction from a well-dated peat core retrieved from the Zhaogongting peatland (abbreviated as ZGT, 26° 24′ 40″ N, 114° 04′ 40″ E; 1790 m above sea level; Fig. 1), located in southeastern China. This site receives moisture sourced from both the Indian Ocean and the western Pacific Ocean (Tan 2014). Based on data from the nearby Hengyang Meteorological Station (26° 32′ 24″ N, 114° 54′ E; 105 m above sea level), 67% of the annual rainfall occurs during May–August. Peatlands of southeastern China are dispersed in intermontane basins, and are ideally suited to reconstruct the Holocene hydroclimate evolution. These carbon-rich archives facilitate high-resolution AMS ^{14}C dating, and contain biomarkers that are sensitive to hydrological conditions (Xie et al. 2013). Indeed, over recent decades, lipids preserved in peat deposits have been shown to track paleohydrological fluctuations in peatlands around the world, including those located within the Asian summer monsoon regions (Xie et al. 2013; Huang et al. 2018). In addition, the specific δ^2H of these lipid biomarkers provide useful information about the moisture changes at the same time of deposition (Huang et al. 2018). In this study, we applied multiproxy from the ZGT peat deposit to reconstruct hydroclimate changes, tracked the changes of precipitation isotope composition using leaf wax δ^2H, and then unveiled the underlying mechanisms modulating the East Asian summer monsoon during the Holocene.

2 Materials and methods

2.1 Site descriptions and sampling

The ZGT peatland is a small subalpine mire developing in the head source of a stream in the Yanling County, Hunan Province. The bedrock surrounding the peatland is dominated by granite. The zonal vegetation of this region is evergreen broadleaved forests. Due to the altitude effect, vegetation in the mountain top is dominated by shrubs, such as *Camellia caudata*, *Rhoddendronkiang* spp. (Han

Fig. 1 Locations of the Zhaogongting peatland and other sites mentioned in the text. 1: Dali Lake (Goldsmiths et al. 2017); 2: Gonghai Lake (Chen et al. 2015); 3: Longfeng Cave (Wei et al. 2020); 4: Dajiuhu peatland (Xie et al. 2013; Huang et al. 2018); 5: Haozhu Cave (Zhang et al. 2018); 6: Heshang Cave (Zhu et al. 2017); 7: Jiulongchi (Gao et al. 2019); 8: Dongge Cave (Wang et al. 2005); 9: Shuizhuyang (Wang and Huang 2019); 10: Dahu peat deposit (Zhou et al. 2004); 11: Tham Doun Mai Cave (Griffiths et al. 2020); 12: Bay of Bengal (Contreras-Rosales et al. 2014). The star denotes Zhaogongting peatland (this study). Mean summer (June–July–August) water vapor flux vectors (kg m^{-1} s^{-1}) vertically integrated from the surface to 300 hPa during 1971–2000, modified after Liu et al. (2015)
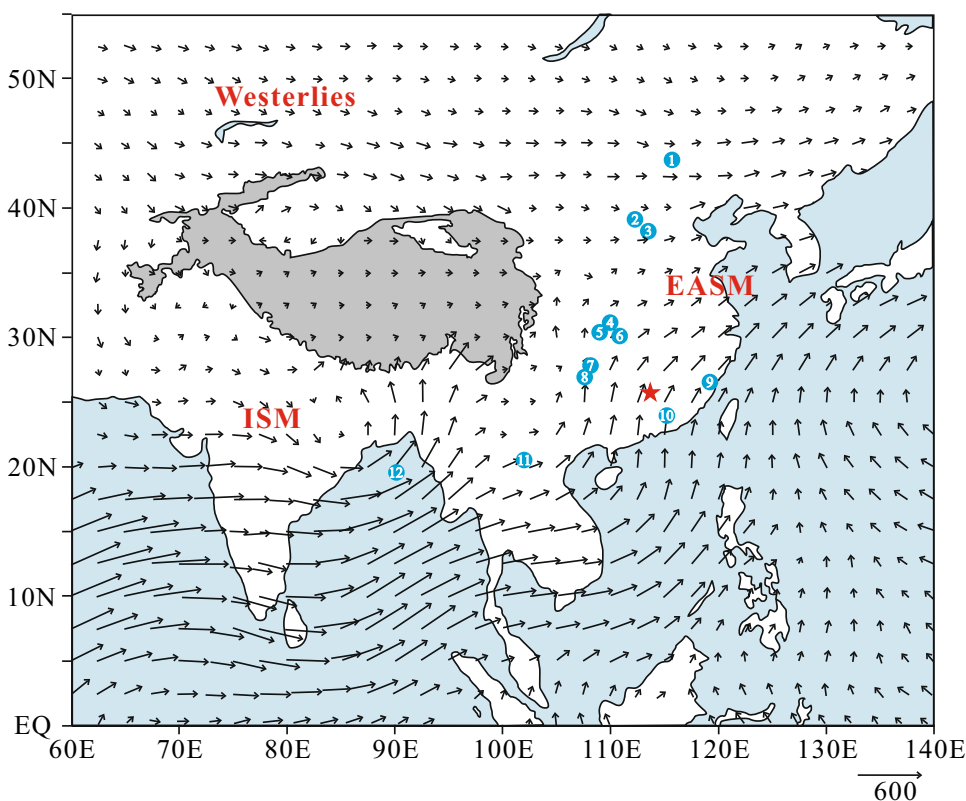
et al. 2016). Within the ZGT peatland, dominant vegetation includes some shrub species, *Carex* spp., *Sphagnum palustre*, and *Polytrichum commune*.

In September, 2016, three 2-m-depth paralleling peat cores (26° 24′ 40″ N, 114° 04′ 40″ E; 1790 m above sea level) were retrieved from the ZGT peatland using a Russian style peat corner. Lithology in these peat cores was near identical and two of them were combined after being sliced at a 1-cm interval in the field. The topmost 4 cm was mainly plant remains. The layer of 4–26 cm consists of black peat, and underlined layer of 26–184 cm was brown peat. From 184 to 188 cm, the peat generally transited to gavel enclosed sediments, with obvious grey cross bedding. The layer of 188–200 cm is gravel enclosed sediments lying on the bedrock. The peat samples were stored in -20 ℃ condition once transferred to the laboratory. For the analysis of dry bulk density, a new 175 cm core was retrieved in the site near the cores of 2016. This new core has a brown peat layer of 150 cm and a 25-cm sediment layer (Table 1).

2.2 Radiocarbon dating

In the laboratory, plant remains (mainly leaves, seeds and shoots) from 19 samples were selected for the radiocarbon analysis. After checking under the microscopy, these dating materials were sent to Beta Analytic Inc for radiocarbon dating analysis. The conventional ^{14}C data were calibrated into

the calendar age using the Bacon age-depth model (Blaauw et al. 2011).

2.3 Lipid extraction and instrumental analyses

About 1.5 g freeze-dried peat sample (rootlets removed) was ground to pass the 60-mesh sieve, and then was ultrasonically extracted for 10 min (6×) with dichloromethane/methanol (9:1, v/v) as solvent. A mixture of internal standards (androstane and cholanic acid) was added to the sample before solvent extraction. Solvent was removed under reduced pressure. The extract was then fractionated into aliphatic, aromatic and polar fractions using silica gel column chromatography with hexane, hexane/dichloromethane (1:1, v/v), dichloromethane/methanol (1:1, v/v) as the elution solvents, respectively. The polar fraction was further separated into neutral and acidic fractions by saponifying (2 h, 70 °C) with 2 mL of 1 mol/L KOH/methanol solution. The neutral fraction was transferred to trimethylsilyl ethers (TMSs) by reacting with bis(trifluoroacetyl)- trifluoroacetamide, while the acidic fraction was transformed to methyl esters by reacting with BF_3/MeOH solution (14%, v/v).

The aliphatic fraction was analyzed with a Shimadzu GC-2010 gas chromatograph installed with a flame ionization detector. The derivatized neutral and acidic fractions were analyzed with a Hewlett Packard 6890 gas chromatograph interfaced with a Hewlett Packard 5973 mass selective detector. Compound specific hydrogen isotope analyses of *n*-alkanes were determined using a Delta V advantage isotope ratio mass spectrometer. The chromatographic conditions in the above analyses were identical with our previous studies (Huang et al. 2018). To check the system stability for compound specific analyses, the Indiana A6 mixture (C_{16}–C_{30} *n*-alkanes) with known δ^2H values were run between every two samples. Squalane (δ^2H − 167‰) was used as the internal standard. Standard deviation for hydrogen isotope analysis was better than ± 5‰ (standard deviation). Results are reported in the delta notation (‰) relative to the Vienna Standard Mean Ocean Water standard for hydrogen isotope values.

Table 1 Results of AMS ^{14}C dating from the ZGT peat core

Lab code	AMS code	Depth/cm	^{14}C age/error	Cal age (BP)*
ZGT-14	486,391	13.5	90 ± 30	142–22
ZGT-23	470,093	22.5	1550 ± 30	1527–1377
ZGT-25	499,671	24.5	920 ± 30	921–780
ZGT-28	486,392	27.5	4520 ± 30	5194–5051
ZGT-37	477,616	36.5	4470 ± 30	5288–5157
ZGT-47	474,015	46.5	4610 ± 30	5459–5376
ZGT-64	474,016	63.5	5290 ± 30	6183–5991
ZGT-82	474,017	81.5	5770 ± 30	6653–6495
ZGT-92	474,018	91.5	6090 ± 30	7024–6859
ZGT-103	470,095	102.5	6090 ± 30	7024–6859
ZGT-124	470,096	123.5	6980 ± 30	7872–7722
ZGT-128	486,393	127.5	6970 ± 30	7866–7707
ZGT-139	486,394	138.5	6280 ± 30	7264–7165
ZGT-142	477,617	141.5	9290 ± 40	10,586–10,371
ZGT-151	470,097	150.5	9070 ± 30	10,252–10,197
ZGT-160	474,020	159.5	9880 ± 40	11,363–11,214
ZGT-170	477,618	169.5	9690 ± 40	11,211–11,070
ZGT-175	499,672	174.5	11,790 ± 40	13,741–13,538
ZGT-181	470,098	180.5	12,080 ± 40	14,076–13,778

*2 σ error intervals; BP: before the present (1950 AD)

2.4 Analysis of total organic content and dry bulk density

The freeze-dried peat sample was ground to < 100 mesh and homogenized, and then analyzed on the Vario MiCRO cube Element Analyzer to get the total organic content (TOC). The measurement of dry bulk density was conducted on the new core collected in August 2019. This core was quite near the previous core retrieved in 2013 and has a quite similar lithology with the previous one. Samples with certain volume were dried at 50 °C to remove water and then was weighted. The dry bulk density (g m^{-3}) was calculated by

dividing the dry weight by the sample volume. The apparent carbon accumulation rate (CAR, g C m^{-2} year^{-1}) was calculated following Lähteenoja et al. (2012), by multiplying the peat accumulation rate (mm year^{-1}), the dry bulk density (g m^{-3}), and the C content (g C g^{-1} dry weight).

3 Results

3.1 Chronology

Plant residues from 19 peat horizons were selected for radiocarbon dating (Table 1). Based on the Bacon age model, the 184-cm peat layer of the ZGT peat core spans the last 14 ka (Fig. 2). For the whole peat horizon, the sedimentation rates vary greatly. From 184 to 143 cm, the sedimentation rate averages 9.7 cm/kyr. The interval of 143–134 cm also has a quite low sedimentation rate (avg. 4.5 cm/kyr). The interval 134–30 cm has a much higher sedimentation rate (avg. 29.2 cm/kyr), while the uppermost 30 cm has a quite low sedimentation rate (avg. 6.4 cm/kyr). The chronology and sedimentation rates of our peat core are to some extent similar to the results of another nearby peat core retrieved from Jiangxi'ao peatland (26°28′N, 114°05′E, altitude 1650 m),

where the 150-cm peat covered an age of ca. 10.6 ka (Han et al. 2016).

3.2 Organic carbon content and accumulation rate in the peat core

In the ZGT core, the total organic carbon concentration (TOC) ranges from 18.8 to 40.3% and averages 30.4% (1σ 6.6%). The TOC values gradually increase from the bottom 184 cm (14.2 ka) to a depth of ~133–58 cm (8.2–5.9 ka), and then remain relatively low for the rest of the record (Fig. 3a). In the ZGT core, the values of apparent carbon accumulation rate (CAR) fluctuate between 2.3 and 146.5 g C yr^{-1} m^{-2} (avg. 43.7 g C year^{-1} m^{-2}, 1σ 34.4), with the temporal pattern similar to that of TOC (Fig. 3b). Here, the mean value of 0.52 g cm^{-3} was used to calculate the CAR. In the 2019 peat core, the dry bulk density for the upper 150 cm (peat layers) is constant (avg. 0.52 g cm^{-3}, $n = 133$, 1σ 0.09).

3.3 Distributions of molecular and hydrogen isotope compositions of *n*-alkanes

In the ZGT peat core, *n*-alkanes mainly range from C$_{21}$ to C$_{33}$ and show a strong odd-over-even carbon predominance, with the values of carbon preference index

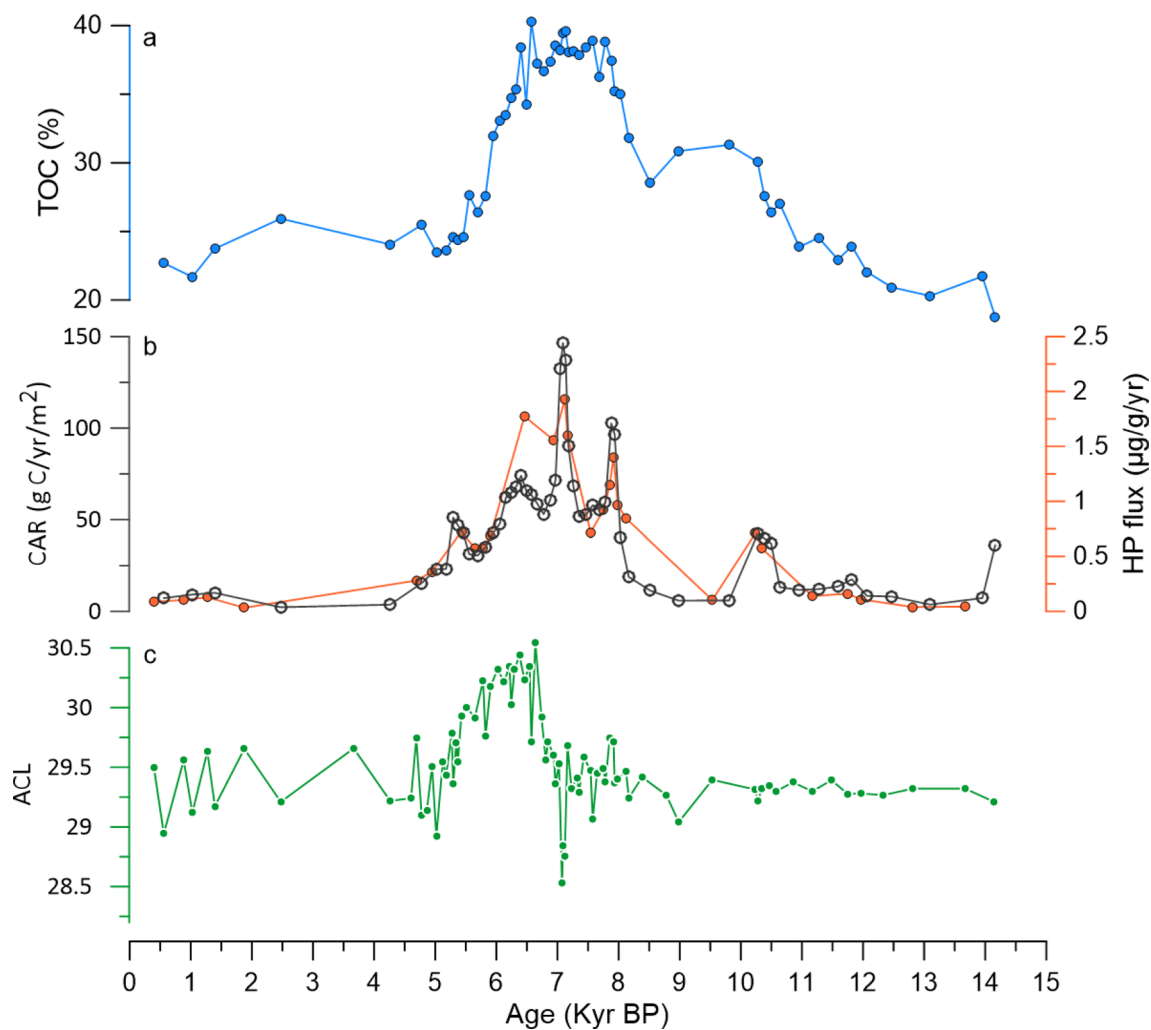**Fig. 2** Chorology of the ZGT peat core retrieved from the Zhaogongting peatland
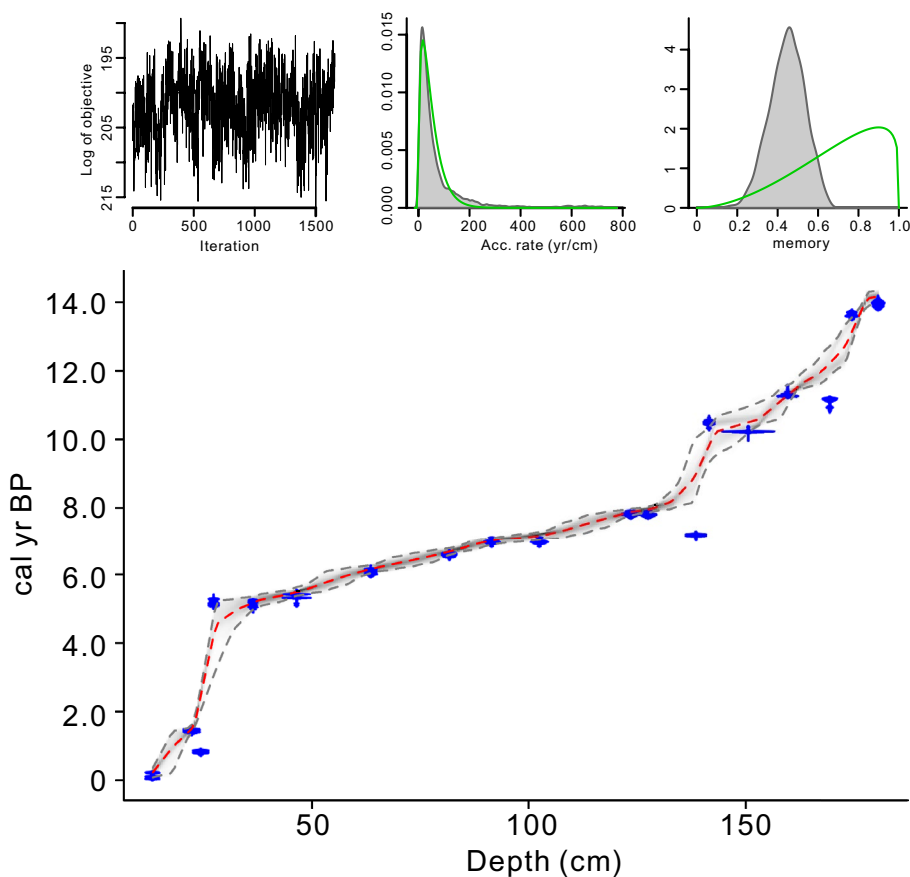
Fig. 3 Downcore profiles of **a** TOC, **b** CAR (blank circle) and the hopanoid flux (filled circle), and **c** ACL

averaging 6.5 (1σ 1.1) for C_{21}-C_{33} homologs. The total concentration of C_{21}-C_{33} n-alkanes varies between 30.1 and 289.1 µg/g dry weight, with a standard deviation of 63.1. Over the whole core, C_{29} and C_{31} n-alkanes are the predominant components and each makes up > 29% of the total n-alkanes. The predominance of the longer homologs is further verified by the quite high average chain length (ACL). In the ZGT core, the ACL values vary between 28.5 and 30.5, with an average of 29.5 and standard deviation (1σ) of 0.4 (Fig. 3c). Throughout the profile, the ACL values remain relatively constant, except for the interval 6.7–5.4 ka (avg. 30.1, 1σ 0.2). In the ZGT peat core, $\delta^2 H_{alk}$ values of n-C_{29} and C_{31} alkanes show a consistently increasing trend from 10 ka until 8 ka (n-C_{29}: avg. – 202‰, 1σ 6‰; C_{31}: avg. – 192‰, 1σ 4‰), and a sharp decrease between 8–7.5 ka (n-C_{29}: avg. – 211‰, 1σ 9‰; C_{31}: avg. – 200‰, 1σ 9‰), and then broadly increase until

5.4 ka (n-C_{29}: avg. – 201‰, 1σ 6‰; C_{31}: avg. – 198‰, 1σ 7‰; Fig. 4c).

3.4 Hopanoids in the peat core

In the ZGT core, geological hopanoids are dominated by hopanes and hopanoic acids, with a minor contribution from hopanols. C_{31} 17α(H), 21β(H) homohopane takes a predominance in hopanes, while hopanoic acids mainly consist of C_{32} 17β (H), 21β(H) and 17α(H), 21β(H) homologs. Such distributions of hopanoids are typical in acidic peats (Xie et al. 2013). The hopanoid flux ranges between 0.03 and 1.93 µg/g/yr and averages 0.65 µg/g/yr (Fig. 3b). These flux values are similar to those reported in Chinese subtropical peatlands (Xie et al. 2013; Wang and Huang 2019). Throughout the ZGT core, the hopanoid flux remains quite low, except for the interval between ~ 8.2 and ~ 5.4 ka (Fig. 3b).

Fig. 4 Moisture isotope comparison from East Asian and Indian monsoon domain. **a** Northern Hemisphere July insolation at 65° N (Berger 1978); **b** Stacked stalagmite $\delta^{18}O$ from China (Yang et al. 2019); **c** Compound-specific hydrogen isotope compositions of n-C_{29} (blue) and n-C_{31} (cyan) alkanes from ZGT (this study); **d** the C_{29} and C_{31} n-alkane weight-averaged δ^2H values from the Bengal Bay (Contreras-Rosales et al. 2014); **e** Stalagmite $\delta^{18}O$ from Laos (Griffiths et al. 2020); **f** Temperature difference between tropical West and East Pacific (Koutavas and Oanides 2012)
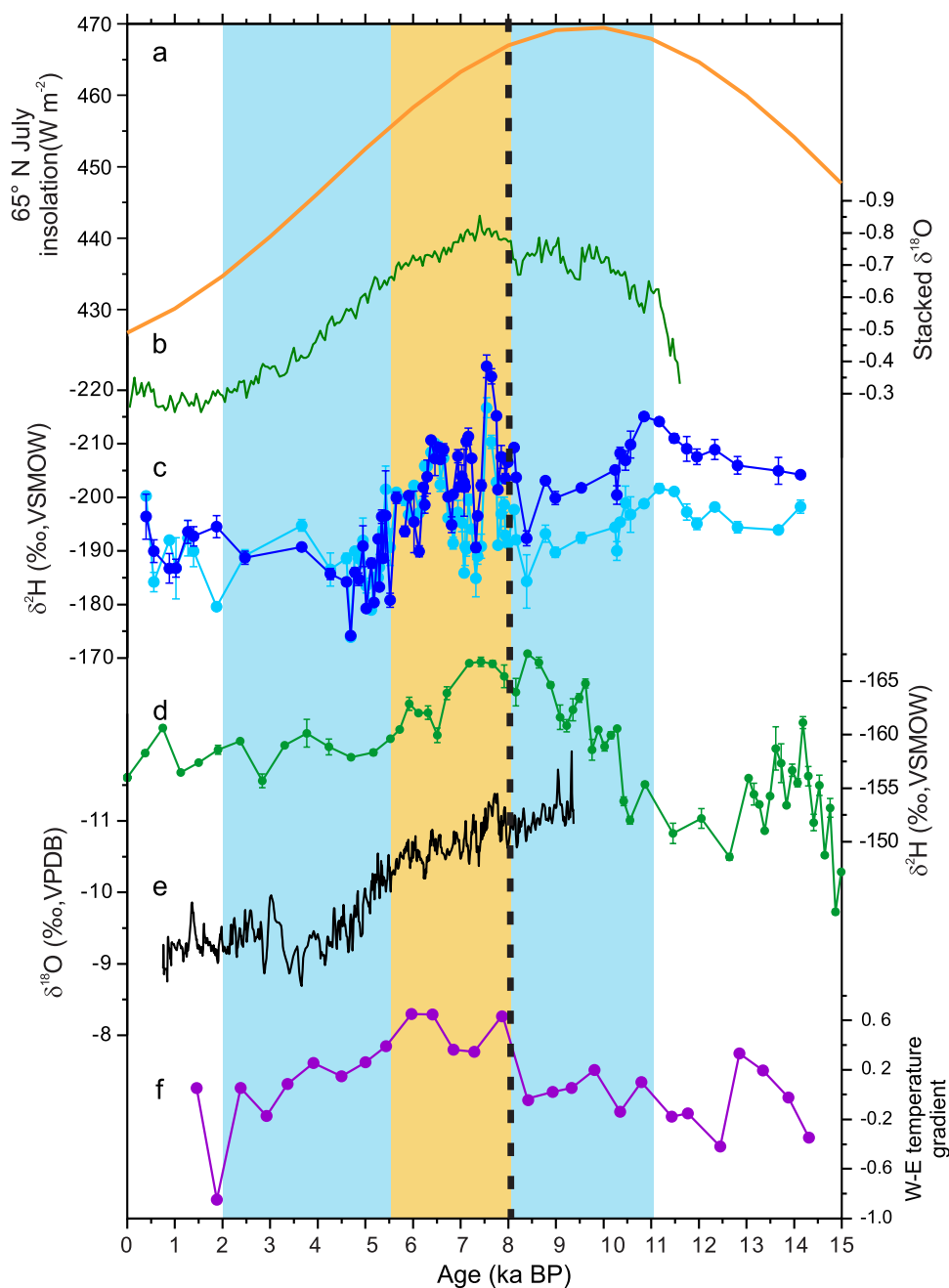
4 Discussion

4.1 Drying mid-holocene recorded in the ZGT peat deposit

In subtropical peatlands like ZGT, CAR and the hopanoid flux are useful in reconstructing paleohydrological conditions. The CAR values are mediated by the TOC content and peat accumulation rate (Lähteenoja et al. 2012). The ZGT peatland was developed in a relatively small intermountain depression, with a small stream flowing through it. Under wetter conditions, increased surface water flow has the tendency to transfer large amounts of detrital material from the surrounding regions, which can dilute the accumulation of organic matter. By contrast, during drier conditions, a drawdown of the water level can facilitate the development of marsh and the accumulation of organic-rich sediments. This interpretation of the carbon accumulation with respect to hydrological conditions is popular in the subalpine peatlands of subtropical China (Zhou et al. 2004; Wang and Huang 2019). Therefore, we posit that the relatively high CAR values in the ZGT core during the period 8–5.4 ka likely reflect a period of enhanced aridity (Fig. 3b).

Hopanoids are abundant in acidic peat samples, and have been interpreted to mainly originate from aerobic bacteria (Xie et al. 2013). The origin of hopanoids from aerobic bacteria has been proven by the evidence of *sqh*C genes in the Dajiuhu peatland, where more than 95% hopanoid-producing bacteria belong to aerobe (Xie et al. 2013; Gong et al. 2015). Herein, higher hopanoid fluxes can be inferred to reflect drier conditions, which favor the dwelling of aerobic bacteria in the uppermost peat horizon. By contrast, lower hopanoid fluxes typically occur during wetter climates, with the prevailing saturated sediment not favorable for aerobes (Xie et al. 2013; Wang and Huang 2019). In light of this interpretation, the increased hopanoid fluxes of the ZGT peat core between ~ 8.2 and ~ 5.4 ka supports the CAR values that this mid-Holocene period was quite dry (Fig. 3b).

A drying mid-Holocene inferred by the ZGT peat core is broadly consistent with the paleohydrological reconstructions from the Dajiuhu peatland (31° 28′ N, 110° 00′ E, altitude 1700 m; Xie et al. 2013; Liu et al. 2019). Results from the Heshang Cave (30° 27′ N, 110° 25′ E, altitude 294 m asl), located to the south of the Dajiuhu peatland, also record mid-Holocene drying (Zhu et al. 2017; Wang et al. 2018). Pollen-based quantitative reconstructions from three lacustrine sequences demonstrated that precipitation declined since 7 ka in the lower Yangtze regions of China (Li et al. 2018b). Moreover, recent work from the Jiulongchi wetland in the Fanjing Mountains (27° 53′ N, 108° 41′ E, altitude 2048 m asl) suggests the occurrence of a drying interval between 8–4.6 ka (Gao et al. 2019). Taken together, these results suggest a widespread drying trend prevailed in the middle and lower reaches of the YRV during the mid-Holocene.

However, there are some minor temporal differences among the above hydroclimate reconstructions. For example, the onset of the drying trend occurs slightly earlier in the more southerly ZGT and Jiulongchi regions (ca. 8 ka) compared to the Dajiuhu peatland, where the trend begins around 7 ka. Such a temporal difference may be the result of the transgression of Asian summer monsoon intensity following the changes in insolation (Zhou et al. 2016). It is also possible that dating uncertainty exerted an influence on this temporal difference.

4.2 Changes in precipitation isotopes inferred from δ^2H_{alk}

Our detailed modern process investigation in the Dajiuhu peatland suggests that the δ^2H values of long-chain *n*-alkanes (δ^2H_{alk}) in the subtropical peatlands of China are mainly controlled by precipitation isotope compositions (δ^2H_p) and plant life forms (Huang and Meyers 2019). In the ZGT peatland, peat-forming plants are dominated by shrub and graminoid species, together with *Polytrichum commune*

and *Sphagnum palustre*. Due to the quite low production of long-chain *n*-alkanes in *P. commune* and *S. palustre* (Zhao et al. 2018), their influence on the ZGT δ^2H_{alk} record should be minor.

Over the interval of 8–5.4 ka, the ACL values, which vary closely with the plant types in peatlands (Zhao et al. 2018), do not follow the general trends of δ^2H_{alk} values (Fig. 4). Furthermore, *n*-alkane homologs from shrub species normally have less depleted δ^2H_{alk} values than those derived from forb and graminoid species (Zhao et al. 2018). Taken together, the influence from changes in plant types does not exert a significant effect on the general increasing trend of δ^2H_{alk} values during the mid-Holocene in the ZGT peat core. Thus, the δ^2H_{alk} values in the ZGT peat core probably mainly reflect the changes of precipitation isotope compositions on centennial timescales. Such an interpretation has been confirmed in lacustrine and peat sequences in the monsoonal regions of China (e.g., Rao et al. 2016; Zhang et al. 2020; Zhao et al. 2021a b).

Such a deduction is also supported by the synchronous decline of ZGT δ^2H_{alk} (Fig. 4c) and the stacked composted stalagmite calcite $\delta^{18}O$ sequence from China (Yang et al. 2019; Fig. 4b) and southeast Asia (Griffiths et al. 2020; Fig. 4e), as well as the δ^2H_{alk} record from the Bay of Bengal (Contreras-Rosales et al. 2014; Fig. 4d), which indicate that the Northern Hemisphere summer insolation (Berger 1978; Fig. 4a) was the dominant control on the moisture composition in East Asian and Indian monsoon domains.

During the early Holocene (~ 10–8 ka), the observed increases in the ZGT δ^2H_{29} and δ^2H_{31} alkanes could be attributed to a reduction in southerly monsoonal winds and Indian monsoon moisture flux as has been shown in previous studies (Wang et al. 2005; Yang et al. 2019), particularly those at 8.2 ka (Cheng et al. 2009), 9.2 ka and 9.5 ka (Fleitmann et al. 2008) identified in the Asian monsoon speleothem records. A potential caveat, however, is the prolonged duration of these weaker monsoon intervals as revealed in ZGT could, at least in part, be explained by the lower sedimentation rate or possible deposit missing and corresponding lower sampling resolution. Meanwhile, given the strong similarity between ZGT δ^2H_{29} record and West–East Pacific temperature gradient (Koutavas and Joanides 2012; Fig. 4f), the Western North Pacific sourced moisture (enriched in ^{18}O and ^2H) flux may also contribute the enriched ZGT δ^2H signal in southeast China, especially with frequent El Niño events during the Early Holocene (Tan 2014; Zhu et al. 2017).

4.3 Hydroclimate changes and the possible forcings during the Holocene

The paired records of moisture and hydroclimate presented here help delineate the timing and spatial variation

of hydroclimate fluctuations in southeast China since the late deglacial. Consistent with the previous speleothem based hydroclimate reconstruction from Haozhu Cave in the middle and lower Yangtze Valley during the late deglacial (Fig. 5e; Zhang et al. 2018), the bottom ^{14}C dates and higher CAR/HP flux from ZGT peatland indicate two relative drying intervals during the Bølling-Allerød and the early Holocene following the abrupt Younger Dryas termination, whereas the lower sediment rate or possible deposit missing, coupled with lower CAR and HP flux indicate a strong erosion and corresponding wet hydroclimate during the Younger Dryas and the time interval between 10 to 8 ka. Thus, we generally follow the interpretation by Zhang et al. (2018) for the hydroclimate change during the last deglacial and early Holocene.

For the time interval before ~ 8 ka, the estimated sea level was much lower than present-day (Lambeck et al. 2014) because of the large volumes of ice sheets in the high northern latitudes. Gradually increasing summer insolation triggered meltwater pulse into the circum-North Atlantic region (Thornalley et al. 2009; Liu et al. 2014; Fig. 5b, c) that weakened the Atlantic meridional overturning circulation (AMOC, Bamberg et al. 2010; McManus et al. 2004; Hou et al. 2011). A weakened AMOC increased the meridional temperature gradient (Hou et al. 2011), leading to a southward displacement of the westerly jet, which in turn led to a prolonged Mei-yu and shortened Midsummer stage (Kong et al. 2017; Zhang et al. 2018), with increased rainfall over central and southeastern China (Fig. 5e) and reduced rainfall over northeastern (Chen et al. 2015; Goldsmith et al. 2017; Fig. 5d). Furthermore, the overall wetter conditions during the 10–8 ka period in central China could be attributable to a higher frequency in the El Niño events associated with a lower W-E Pacific temperature gradient (Zhu et al. 2017; Koutavas and Joanides 2012; Fig. 5f). When El Niño-like conditions dominated, the western Pacific subtropic high (WPSH) would have extended both westwards and southwards, coupled with southward shift of the westerly winds, impeding the northward advance of the EASM rain belt and strengthened early summer rainband along the central and southeastern China, thus leading to decreased rainfall in northern China and increased rainfall in the YRV and southeast China (Tan 2014; Kong and Chiang 2020). A notable uncertainty in the early Holocene portion of the ZGT profile, however, is the possible occurrence of some short-lived dry intervals that were not preserved in the record due to the potential for erosion of older sediments by abrupt increases in rainfall, as recorded by the discontinuous AMS ^{14}C data clusters over this interval (Fig. 2).

At ~ 8 ka, when the sea level reached a near stable state (Lambeck et al. 2014), the influence of North Atlantic meltwater on the AMOC was likely overridden by the strong insolation forcing, and the Asian monsoon reached its peak strength shortly thereafter (Figs. 4 and 5f). Higher insolation warms the high northern latitudes, which in turn decreases the equator-to-pole temperature gradient (Kaufman et al. 2020). As a result, the westerly jet quickly shifts northward, leading to stronger low-level southern monsoonal flow, and the advection of more remote Indian Ocean moisture (depleted in [18]O and ^{2}H) penetrated deeper into central and northern China (Chiang et al. 2015; Zhang et al. 2018), imprinted clearly into the speleothem and ZGT record (Fig. 4). An earlier northward positioning of the westerlies relative to the Tibetan Plateau, leads to an earlier termination and shorter (prolonged) Mei-yu (Midsummer stage) stage (Kong et al. 2017), drying central and southeastern China (Fig. 5e) and wetting the northern China (Fig. 5d). Meanwhile, increased W-E Pacific temperature gradient (Koutavas and Joanides 2012), and thus a La Niña-like condition dominated in the tropical Pacific Ocean during this period. As the WPSH weakened and retreated northeastwards, more moisture transports along the northwest edge of the WPSH to northern China, leading to increased rainfall in northern China and decreased rainfall in the YRV and southeastern China (Tan 2014).

After ~ 8 ka, the gradually enriched δ^2H and $\delta^{18}O$ records suggest a gradual weakening of the Asian summer monsoon (Fig. 4), which generally follows the decreasing summer insolation (Berger 1978) and southward migration of the intertropical convergence zone (Haug et al. 2001). This monsoon weakening trend, however, is not entirely synchronous with the changes in hydroclimate across China. The hydrological proxies show that while southeast China exhibited an overall drying trend from ~ 8–5.2 ka (Fig. 5e), northern China exhibited persistent wetter conditions until around 5 ka (Fig. 5d) when the whole region exhibited an abrupt hydroclimate reversal almost synchronously from north to south China. We argue that, to an extent, this large-scale hydroclimate transition during the early and middle Holocene in monsoonal eastern China can be attributed to the final breakup of the northern ice sheets (Lambeck et al. 2014) and weakened AMOC (McManus et al. 2004), which probably outweighed the influence of summer insolation during this period. For instance, the period from ~ 8–5 ka was marked by a decreasing summer insolation trend, though northern (southern) China actually became wetter (drier).

Following the drier conditions in southeastern China during the mid-Holocene, the hydroclimate in ZGT abruptly returns to a wetter mean state after ~ 5 ka (Fig. 5e). In contrast, in northern and southern Asia, the hydroclimate transitioned to an overall drier mean state around this time (Fig. 5d, g). It is possible that this transition to wetter conditions in southeastern China was, at least in part, a result of declining summer insolation (Berger 1978), which acted to increase the polar-equator temperature gradient, leading to the overall southward

Fig. 5 Paleohydrological comparisons among records of the eastern monsoon region of China. **a** Northern Hemisphere July insolation at 65° N (Berger 1978); **b** Synthesized meltwater flux in the Northern Hemisphere (Liu et al. 2014); **c** Dinocyst-assemblage salinity estimates from central Labrador Sea, high/low salinity corresponding to strong/weak AMOC (Thornalley et al. 2009); **d** Hydroclimate changes in northern China from Dali Lake elevation reconstruction (Goldsmith et al. 2017), Longfeng cave speleothem growth frequency (Wei et al. 2020) and a regionally synthesized PANN (Li et al. 2018a); **e** Hydroclimate changes in central and southeastern China, the hopanoid flux and CAR from ZGT (this study), the HZZ PC1 of Haozhu cave (Zhang et al. 2018); **f** Compound-specific hydrogen isotope composition of n-C_{29} alkanes from ZGT, the horizontal points and error bars referring the AMS ^{14}C dating (this study); **g** Composite speleothem δ^{13}C record from Laos (Griffiths et al. 2020); **h** Dust flux records North African continental slope cores (McGee et al. 2013); **i** δ^2H_{wax} records from East Africa and the timing of Green Sahara (Tierney and deMenocal 2013)
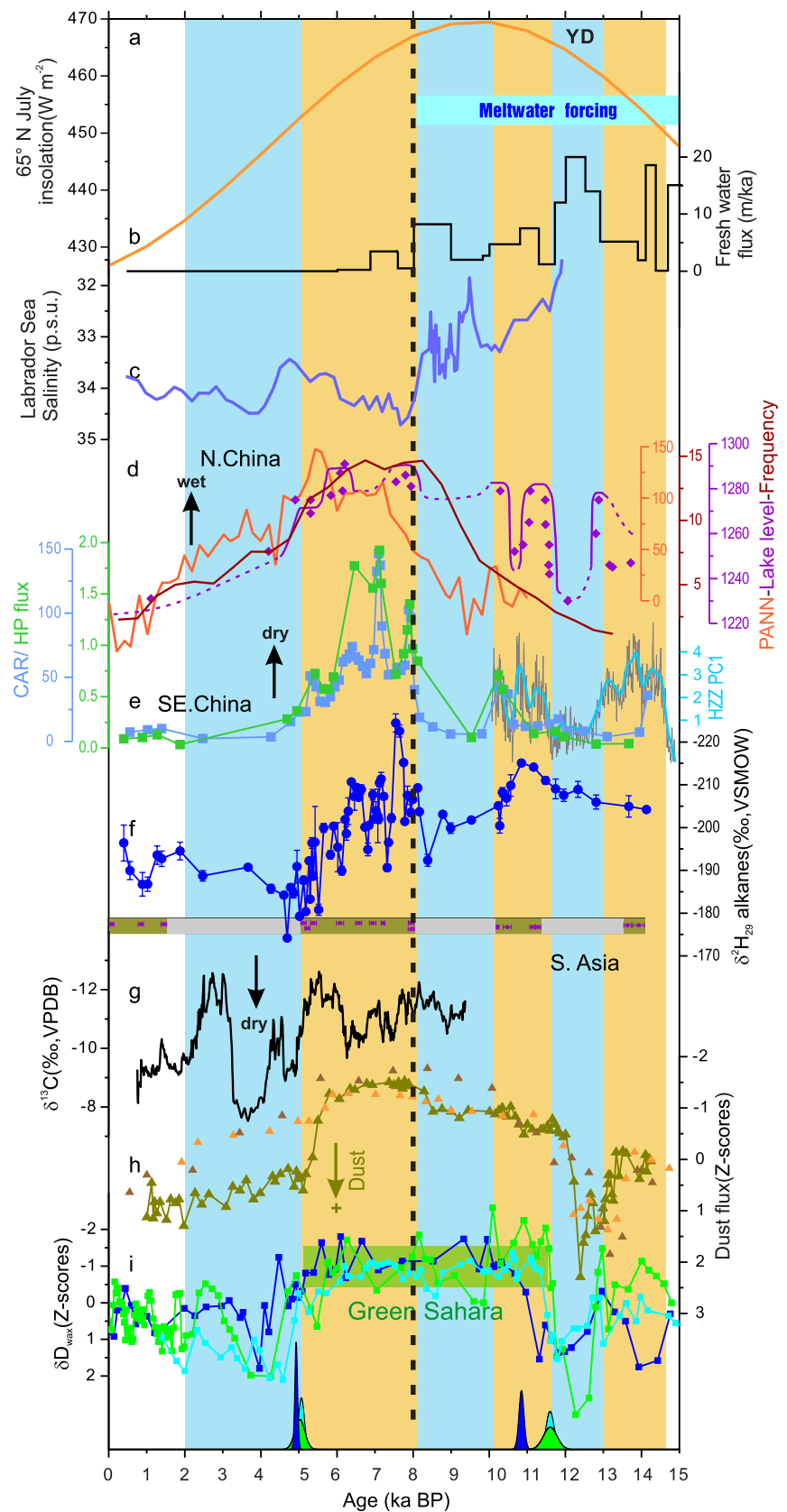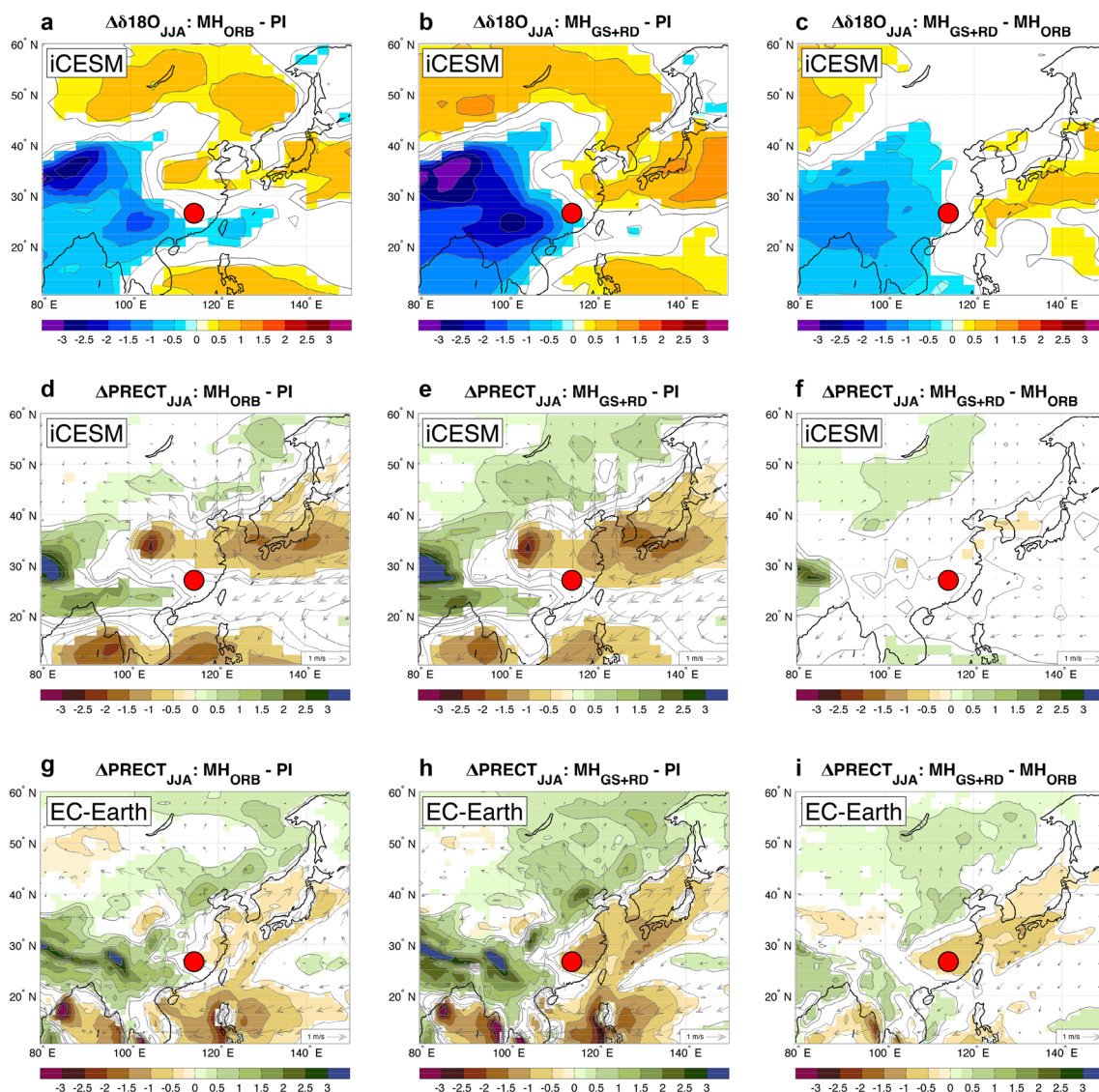
Fig. 6 iCESM and EC-Earth simulated changes in mid-Holocene (MH) East Asia summer precipitation and δ^{18}O. **a–f** iCESM (Tabor et al. 2020) and (**g–i**) EC-Earth (Piao et al. 2020) simulated mid-

Holocene (MH) summer precipitation and δ^{18}O anomalies between standard MH simulation (MH$_{OB}$), greener Saharan vegetation and reduced dust feedbacks (MH$_{GS+RD}$) and control simulation (PI)

displacement of the westerly jet and in turn prolonged (shorter) Mei-yu (Midsummer) stage (Kong et al. 2017) that increased (reducing) rainfall in central and southeastern (northern) China. However, the non-linear nature of the hydroclimate changes at ~5 ka with respect to the monotonic changes in insolation suggests that insolation was not the sole driver of hydroclimate variability.

Recent work has shown that climate teleconnections associated with Saharan dust and vegetation climate feedbacks can amplify the insolation forcing of tropical monsoons through the Holocene (Pausata et al. 2017; Griffiths et al. 2020; Piao et al. 2020; Tabor et al. 2020). Indeed, our proxy results suggest a tight connection between the East Asian hydroclimate and Saharan dust (McGee et al. 2013)

and vegetation (Tierney and deMenocal 2013) changes, particularly at the end of the African Humid Period around 5 ka, which aligns with the rapid shift from dry to wet conditions in southeastern China (Fig. 5e). Importantly, this interpretation is consistent with recent modeling studies. Results from two different Middle Holocene (MH) climate model sensitivity experiments—i.e., iCESM (Tabor et al. 2020) and EC-Earth (Piao et al. 2020)—show that a MH green Sahara (MH$_{GS+RD}$) leads to a more northward penetration of the EASM compared with a MH experiment imposing pre-industrial dust and vegetation boundary conditions over Northern Africa (MH$_{ORB}$). The key hydroclimatic feature of these MH$_{GS+RD}$ anomalies (relative to MH$_{ORB}$) is the development of a tri-pole pattern of rainfall variability

characterized by increased rainfall over Indochina and northeastern China, and decreased precipitation in the central- and south-eastern China (Griffiths et al. 2020; Fig. 6f, i). These MH$_{GS+RD}$ rainfall anomalies (relative to MH$_{ORB}$) across China can best be explained by a strengthening of the Western Pacific Subtropical High (WPSH) due to a westward and intensified shift of the Walker circulation (Pausata et al. 2017), which acted to increase the strength of the Hadley circulation via anomalous surface ocean heating of the east Indian Ocean (Piao et al. 2020).

The embedded water isotope module in iCESM also simulates more depleted δ^{18}O of precipitation in central and southern China associated with greener Sahara conditions (Tabor et al. 2020; Fig. 6c) in agreement with paleoclimate archives from the region, including our record (Fig. 4). In the iCESM MH$_{GS+RD}$ experiments, a vegetated Sahara intensifies and extends the African Monsoon northward, which leads to more depleted δ^{18}O of water vapor being drawn into the Indian Monsoon region and in turn interior China (Tabor et al. 2020). As noted above, the MH$_{GS+RD}$ experiments show a strengthening of the WPSH via a westward shift of the Walker circulation. Combined with increased ^{18}O-depleted source moisture from India and Tibet, and anomalous warming in Northeastern China, the consequent of a strengthened WPSH was a greater incursion of δ^{18}O depleted moisture from the south and west relative to higher δ^{18}O from Pacific sources (Tabor et al. 2020).

5 Conclusion

We have provided a novel record of hydroclimate variability from southeastern China during the last deglaciation and Holocene. Our new δ^2H record reveals a relatively weaker EASM during the early (10 to 8 ka) and late Holocene (after 5.4 ka), while a stronger EASM during the mid-Holocene between ~ 8 and ~ 5.4 ka. However, proxies of local hydroclimate from the same core reveal an opposing pattern—i.e., overall wetter (drier) conditions during the early/late (mid-) Holocene. Aligning with previous work from nearby Haozhu Cave (Zhang et al. 2018), our new results show a dominant control of summer insolation and North Atlantic freshwater forcing on millennial-scale EASM variability and hydroclimate changes during the last deglaciation and early Holocene. These forcings alone, however, cannot explain the extreme drought conditions observed in southeastern China during the mid-Holocene when the EASM was generally stronger. Through multiproxy comparisons with records across northern Africa (McGee et al. 2013;Tierney and deMenocal 2013), combined with existing isotope-enabled coupled climate model simulations (Griffiths et al. 2020; Piao et al. 2020; Tabor et al. 2020; Tabor et al. 2020), we instead show

that climate feedbacks associated with increased vegetation and reduced dust loads during the "Green Sahara Period" acted to *amplify* the insolation-driven millennial megadrought interval in southeastern China, in concert with pluvial conditions in northern China due to enhanced summer monsoon circulation. In line with recent studies (Griffiths et al. 2020; Piao et al. 2020; Tabor et al. 2020), these findings therefore suggest that vegetation-dust climate feedbacks played a critical role in modulating the orbital-paced changes in monsoon circulation and regional hydroclimate across East Asia during the Holocene.

Declarations

References

Bamberg A, Rosenthal Y, Paul A, Heslop D, Mulitza S, Rühlemann C, Schulz M (2010) Reduced North Atlantic Central Water formation in response to early Holocene ice-sheet melting. Geophys Res Lett 37:L17705

Berger A (1978) Long-term variations of daily insolation and Quaternary climatic changes. J Atmos Sci 35:2362–2367

Blaauw M, Christen JA (2011) Flexible paleoclimate age-depth models using an autoregressive gamma process. Bayesian Anal 6:457–474

Chen F, Xu Q, Chen J, Birks HJB, Liu J, Zhang S, Jin L, An C, Telford RJ, Cao X, Wang Z, Zhang X, Selvaraj K, Lu H, Li Y, Zheng Z, Wang H, Zhou A, Dong G, Zhang J, Huang X, Bloemendal J, Rao Z (2015) East Asian summer monsoon precipitation variability since the last deglaciation. Sci Rep 5:11186

Cheng H, Fleitmann D, Edwards RL, Wang X, Cruz FW, Auler AS, Mangini A, Wang Y, Kong X, Burns SJ, Matter A (2009) Timing and structure of the 8.2 kyr BP event inferred from δ^{18}O

records of stalagmites from China, Oman, and Brazil. Geology 37:1007–1010

Cheng H, Zhang H, Zhao J, Li H, Ning Y, Kathayat G (2019) Chinese stalagmite paleoclimate researches: a review and perspective. Sci Chin Earth Sci 62(10):1489–1513

Chiang JCH, Fung IY, Wu CH, Caid Y, Edman JP, Liu Y, Day JA, Bhattacharya T, Mondal Y, Labrousse CA (2015) Role of seasonal transitions and westerly jets in East Asian paleoclimate. Quat Sci Rev 108:111–129

Contreras-Rosales LA, Jennerjahn T, Tharammal T, Meyer V, Lückge A, Paul A, Schefuß E (2014) Evolution of the Indian Summer Monsoon and terrestrial vegetation in the Bengal region during the past 18 ka. Quat Sci Rev 102:133–148

Fleitmann D, Mudelsee M, Burns SJ, Bradley RS, Kramers J, Matter A (2008) Evidence for a widespread climatic anomaly at around 9.2 ka before present. Paleoceanography 23:PA1102.

Gao Y, Xiong K, Quan M, Song B, Peng H, Peng H, Shen W, Bao K (2019) Holocene climate dynamics derived from pollen record of Jiulongchi wetland in Fanjing Mountain, southwest China. Quat Inter 513:1–7

Goldsmith Y, Broecker WS, Xu H, Polissar PJ, deMenocal PB, Porat N, Lan JH, Cheng P, Zhou WJ, An ZS (2017) Northward extent of East Asian monsoon covaries with intensity on orbital and millennial timescales. Proc Natl Acad Sci USA 114:1817–1821

Gong L, Wang H, Xiang X, Qiu X, Liu Q, Wang R, Zhao R, Wang C (2015) pH shaping the composition of sqhC-containing bacterial communities. Geomicrobiol J 32:433–444

Griffiths ML, Johnson KR, Pausata FSR, White JC, Henderson GM, Wood CT, Yang H, Ersek V, Conrad C, Sekhon N (2020) End of Green Sahara amplified mid- to late Holocene megadroughts in mainland Southeast Asia. Nat Commun 11:4204

Han A, Zeng L, Huang K, Liao W, Zheng Z, Chen C (2016) Holocene climate records from a mountain wetland in Luoxiao ranges. Trop Geogr 36(3):477–485 (**(in Chinese with English abstract)**)

Haug GH, Hughen KA, Sigman DM, Peterson LC, Röhl U (2001) Southward migration of the intertropical convergence zone through the Holocene. Science 293:1304–1308

Hou J, Huang Y, Shuman BN, Oswald WW, Foster DR (2011) Abrupt cooling repeatedly punctuated early-Holocene climate in eastern North America. Holocene 22:525–529

Hu C, Henderson GM, Huang J, Xie S, Sun Y, Johnson KR (2008) Quantification of Holocene Asian monsoon rainfall from spatially separated cave records. Earth Planet Sci Lett 266:221–232

Huang X, Meyers PA (2019) Assessing paleohydrologic controls on the hydrogen isotope compositions of leaf wax n-alkanes in Chinese peat deposits. Palaeogeogr Palaeoclimatol Palaeoecol 516:354–363

Huang X, Pancost RD, Xue J, Gu Y, Evershed RP, Xie S (2018) Response of carbon cycle to drier conditions in the mid-Holocene in central China. Nat Commun 9:1369

Kaufman D, McKay N, Routson C, Erb M, Dätwyler C, Sommer PS, Heiri O, Davis B (2020) Holocene global mean surface temperature, a multi-method reconstruction approach. Sci Data 7:201

Kong W, Swenson LM, Chiang JCH (2017) Seasonal transitions and the westerly jet in the Holocene East Asian summer monsoon. J Clim 30:3343–3365

Kong W, Chiang JCH (2020) Southward shift of Westerlies intensifies the East Asian early summer rainband following El Niño. Geophys Res Lett 47:e2020GL088631.

Koutavas A, Joanides S (2012) El Niño-Southern Oscillation extrema in the Holocene and Last Glacial Maximum. Paleoceanography 27:PA4208.

Lähteenoja O, Reategui YR, Räsänen M, del Castillo TD, Oinonen M, Page SE (2012) The large Amazonian peatland carbon sink in the subsiding Pastaza-Marañón foreland basin, Peru. Glob Change Biol 18:164–178

Lambeck K, Rouby H, Purcell A, Sun Y, Sambridge M (2014) Sea level and global ice volumes from the Last Glacial Maximum to the Holocene. Proc Natl Acad Sci USA 111:15296–15303

Li J, Dodson J, Yan H, Wang W, Innes JB, Zong Y, Zhang X, Xu Q, Ni J, Lu F (2018a) Quantitative Holocene climatic reconstructions for the lower Yangtze region of China. Clim Dyn 50:1101–1113

Li J, Yan H, Dodson J, Xu Q, Sun A, Cheng B, Li C, Ni J, Zhang X, Lu F (2018b) Regional-scale precipitation anomalies in northern China during the Holocene and possible impact on prehistoric demographic changes. Geophys Res Lett 45:12477–12486

Liu Z, Wen X, Brady EC, Otto-Bliesner B, Yu G, Lu H, Cheng H, Wang Y, Zheng W, Ding Y, Edwards RL, Cheng J, Liu W, Yang H (2014) Chinese cave records and the East Asia summer monsoon. Quat Sci Rev 83:115–128

Liu J, Chen J, Zhang X, Li Y, Rao Z, Chen F (2015) Holocene East Asian summer monsoon records in northern China and their inconsistency with Chinese stalagmite δ18O records. Earth-Sci Rev 148:194–208

Liu H, Gu Y, Huang X, Yu Z, Xie S, Cheng S (2019) A 13,000-year peatland palaeohydrological response to the ENSO-related Asian monsoon precipitation changes in the middle Yangtze Valley. Quat Sci Rev 212:80–91

Lu H, Yi S, Liu Z, Mason JA, Jiang D, Cheng J, Stevens T, Xu Z, Zhang E, Jin L, Zhang Z, Guo Z, Wang Y, Otto-Bliesner B (2013) Variation of East Asian monsoon precipitation during the past 21 ky and potential CO$_2$ forcing. Geology 41:1023–1026

McGee D, deMenocal PB, Winckler G, Stuut JBW, Bradtmiller LI (2013) The magnitude, timing and abruptness of changes in North African dust deposition over the last 20,000 yr. Earth Planet Sci Lett 371–372:163–176

McManus J, Francois R, Gherardi J-M, Keigwin L, Brown-Leger S (2004) Collapse and rapid resumption of Atlantic meridional circulation linked to deglacial climate changes. Nature 428:834–837

Pausata FSR, Zhang Q, Muschitiello F, Lu Z, Chafik L, Niedermeyer EM, Stager JC, Cobb KM, Liu Z (2017) Greening of the Sahara suppressed ENSO activity during the mid-Holocene. Nat Commun 8:16020

Piao J, Chen W, Wang L, Pausata FSR, Zhang Q (2020) Northward extension of the East Asian summer monsoon during the mid-Holocene. Glob Planet Chang 184:103046

Rao Z, Li Y, Zhang J, Jia G, Chen F (2016) Investigating the long-term palaeoclimatic controls on the δD and δ18O of precipitation during the Holocene in the Indian and East Asian monsoonal regions. Earth-Sci Rev 159:292–305

Tabor C, Otto-Bliesner B, Liu Z (2020) Speleothems of South American and Asian Monsoons influenced by a Green Sahara. Geophys Res Lett 47:e2020GL089695.

Tan M (2014) Circulation effect: response of precipitation δ18O to the ENSO cycle in monsoon regions of China. Clim Dyn 42:1067–1077

Thornalley DJ, Elderfield H, McCave IN (2009) Holocene oscillations in temperature and salinity of the surface subpolar North Atlantic. Nature 457:711–714

Tierney JE, deMenocal PB (2013) Abrupt shifts in Horn of Africa hydroclimate since the Last Glacial Maximum. Science 342:843–846

Wang Y, Cheng H, Edwards RL, He Y, Kong X, An Z, Wu J, Kelly MJ, Dykoski CA, Li X (2005) The Holocene Asian monsoon: links to solar changes and North Atlantic climate. Science 308:854–857

Wang P, Wang B, Cheng H, Fasullo J, Guo Z, Kiefer T, Liu Z (2017) The global monsoon across time scales: Mechanisms and outstanding issues. Earth-Sci Rev 174:84–121

Wang C, Bendle JA, Zhang H, Yang Y, Liu D, Huang J, Cui J, Xie S (2018) Holocene temperature and hydrological changes reconstructed by bacterial 3-hydroxy fatty acids in a stalagmite from central China. Quat Sci Rev 192:97–105

Wang X, Huang X (2019) Paleohydrological changes in southeastern China from 13.1 to 2.5 ka based on a multi-proxy peat record. Palaeogeogr Palaeoclimatol Palaeoecol 534:109282

Wei Y, Cai Y, Cheng X, Xue G, Lu Y, Ma L, Huang S, He M, Cheng H, Edwards RL (2020) Holocene and deglaciation hydroclimate changes in northern China as inferred from stalagmite growth frequency. Glob Planet Change 195:103360

Xie S, Evershed RP, Huang X, Zhu Z, Pancost RD, Meyers PA, Gong L, Hu C, Huang J, Zhang S, Gu Y, Zhu J (2013) Concordant monsoon-driven postglacial hydrological changes in peat and stalagmite records and their impacts on prehistoric cultures in central China. Geology 41:827–830

Yang X, Yang H, Wang B, Huang L, Shen CC, Edwards RL, Cheng H (2019) Early-Holocene monsoon instability and climatic optimum recorded by Chinese stalagmites. Holocene 29:1059–1067

Zhang H, Griffiths ML, Chiang JCH, Kong W, Wu S, Atwood A, Huang J, Cheng H, Ning Y, Xie S (2018) East Asian hydroclimate modulated by the position of the westerlies during Termination I. Science 362:580–583

Zhang C, Zhao C, Yu Z, Zhang H, Zhou A, Zhang X, Feng X, Sun X, Shen J (2020) Western Pacific Ocean influences on monsoon precipitation in the southwestern Chinese Loess Plateau since the mid-Holocene. Clim Dyn 54:3121–3134

Zhao B, Zhang Y, Huang X, Qiu R, Zhang Z, Meyers PA (2018) Comparison of n-alkane molecular, carbon and hydrogen isotope compositions of different types of plants in the Dajiuhu peatland, central China. Org Geochem 124:1–11

Zhao C, Rohling EJ, Liu Z, Yang X, Zhang E, Cheng J, Liu Z, An Z, Yang X, Feng X, Sun X, Zhang C, Yan T, Long H, Yan H, Yu Z, Liu W, Yu S, Shen J (2021b) Possible obliquity-forced warmth in southern Asia during the last glacial stage. Sci Bull 66:1136–1145

Zhao C, Cheng J, Wang J, Yan H, Leng C, Zhang C, Feng X, Liu W, Yang X. Shen J (2021a) Paleoclimate significance of reconstructed rainfall isotope changes in Asian Monsoon region. Geophys Res Lett 48: e2021aGL092460.

Zhou W, Yu X, Jull AJT, Burr G, Xiao JY, Lu X, Xian F (2004) High-resolution evidence from southern China of an early Holocene optimum and a mid-Holocene dry event during the past 18,000 years. Quat Res 62:39–48

Zhou X, Sun L, Zhan T, Huang W, Zhou X, Hao Q, Wang Y, He X, Zhao C, Zhang J, Qiao Y, Ge J, Yan P, Yan Q, Shao D, Chu Z, Yang W, Smol JP (2016) Time-transgressive onset of the Holocene Optimum in the East Asian monsoon region. Earth Planet Sci Lett 456:39–46

Zhu Z, Feinberg JM, Xie S, Bourne MD, Huang C, Hu C, Cheng H (2017) Holocene ENSO-related cyclic storms recorded by magnetic minerals in speleothems of central China. Proc Natl Acad Sci USA 114:852–857